phys. stat. sol. (a) 98, 91 (1986)

Subject classification: 61.40; S1.61

Institute of Solid State Physics, Academia Sinica, Hefei[1])

Crystallization of Metallic Glass $Pd_{80}Si_{20}$

By

LI ZONGQUAN[2]) and HE YIZHEN

The crystallization behavior of metallic glass $Pd_{80}Si_{20}$ is studied by means of in situ observation during heating in TEM. The crystallization process of $Pd_{80}Si_{20}$ can be divided into four stages: the ordering of atoms in the amorphous matrix, the initial stage of crystallization in which some metastable phases appear at local regions, rapid crystallization in the way of a eutectic reaction, and then metastable phases transformation to a stable phase. The structures of these metastable phases are analysed by means of electron diffraction. Some characteristics of these metastable phases are also discussed.

Das Kristallisationsverhalten von metallischem $Pd_{80}Si_{20}$-Glas wird mittels insitu-Beobachtungen während des Aufheizens im TEM untersucht. Der Kristallisationsprozeß von $Pd_{80}Si_{20}$ läßt sich in vier Stufen teilen: der Ordnungsprozeß der Atome in der amorphen Matrix, der Anfangszustand der Kristallisation, bei dem einige metastabile Phasen in lokalen Bereichen auftreten, schnelle Kristallisation auf dem Wege einer eutektischen Reaktion und dann Übergang dieser metastabilen Phase in eine stabile Phase. Die Strukturen dieser metastabilen Phasen werden mittels Elektronenbeugung analysiert. Einige Charakteristiken dieser metastabilen Phasen werden ebenfalls diskutiert.

1. Introduction

Amorphous Pd–Si alloys have been investigated by various techniques, such as X-ray diffraction, differential scanning calorimetry (DSC), electric resistance measurement, and others [1 to 4] since they were obtained by rapid cooling in 1965 [5]. However, their crystallization process, the structures of metastable phases, and their thermal stability still need to be investigated in detail.

These techniques mentioned above all have their advantages, but also limitations. For example, X-ray diffraction can only give statistical results, but no information on the process of structural trace phases appearing during the initial stage of the crystallization. By transmission electron microscopy (TEM) one cannot only observe the crystallization process directly during heating in TEM but also obtain important information about the local structures of these metastable phases. These metastable phases with the size of about 0.5 μm can be easily analysed by micro-diffraction in TEM. This makes the in situ observation during heating a very useful tool to study in particular the initial stage of crystallization of amorphous alloys.

As a typical material in amorphous Pd–Si alloys, $Pd_{80}Si_{20}$ has been one of the most studied alloys. Masumoto et al. summarized the crystallization process of $Pd_{80}Si_{20}$ as follows [1]: amorphous → incipient stage of crystallization → metastable phase I (f.c.c.) → metastable phase II (complex superstructure) → stable phase (Pd_3Si + Pd). Whereas Duhaj et al. considered the crystallization of $Pd_{80}Si_{20}$ an eutectic reaction, and the eutectic cells consisted of Pd_3Si and Pd_9Si_2. They concluded from their results that

[1]) P. O. Box 29, Hefei, The People's Republic of China.

[2]) Present address: Materials Science Division, Argonne National Laboratory, Argonne, Illinois 60439, USA.

no metastable phases were formed during crystallization [2]. It is the purpose of this work to investigate the crystallization behavior of the metallic glass $Pd_{80}Si_{20}$ by means of in situ observations — how the crystallization takes place and which the structures of these metastable phases are.

2. Experimental

The amorphous $Pd_{80}Si_{20}$ ribbons of about 1.5 mm width and 0.05 mm thickness obtained by the single roller technique [6] were supplied by the Institute of Nobel Metal Research.

The specimens for TEM observation were prepared by the twin jet method with an electrolyte of perchloric acid and methanol solution. The specimens were heated in the TEM chamber (about 1.3×10^{-5} Pa) of a JEM 200-CX at a heating rate of 5 to 10 K/min. When a crystallized area reached a size of 0.5 to 1 μm, which was often a single crystal, the heating current was dropped to zero. After having been cooled to room temperature, the specimen was tilted around the X-axis to get electron diffraction patterns at different tilt angles for structure analysis. Some specimens were heated continuously to higher temperature at which a stable phase had formed.

The analysis of the structures of metastable phases was carried out using the method mentioned in [7]. From two of the diffraction patterns, three noncoplanar reciprocal lattice vectors, $\boldsymbol{g}_1$, $\boldsymbol{g}_2$, and $\boldsymbol{g}_3$, are selected, their magnitudes and angles between them can be easily obtained from the diffraction patterns and the tilt angle. $\boldsymbol{g}_1$, $\boldsymbol{g}_2$, and $\boldsymbol{g}_3$ can be expressed in terms of the reciprocal lattice basis vectors $\boldsymbol{a}^*$, $\boldsymbol{b}^*$, and $\boldsymbol{c}^*$,

$$\begin{aligned} \boldsymbol{g}_1 &= h_1\boldsymbol{a}^* + k_1\boldsymbol{b}^* + l_1\boldsymbol{c}^*, \\ \boldsymbol{g}_2 &= h_2\boldsymbol{a}^* + k_2\boldsymbol{b}^* + l_2\boldsymbol{c}^*, \\ \boldsymbol{g}_3 &= h_3\boldsymbol{a}^* + k_3\boldsymbol{b}^* + l_3\boldsymbol{c}^*. \end{aligned} \tag{1}$$

Reversely, the reciprocal lattice basis vectors can be expressed using these selected reciprocal lattice vectors $\boldsymbol{g}_1$, $\boldsymbol{g}_2$, and $\boldsymbol{g}_3$,

$$\begin{aligned} \boldsymbol{a}^* &= H_1\boldsymbol{g}_1 + K_1\boldsymbol{g}_2 + L_1\boldsymbol{g}_3, \\ \boldsymbol{b}^* &= H_2\boldsymbol{g}_1 + K_2\boldsymbol{g}_2 + L_2\boldsymbol{g}_3, \\ \boldsymbol{c}^* &= H_3\boldsymbol{g}_1 + K_3\boldsymbol{g}_2 + L_3\boldsymbol{g}_3, \end{aligned} \tag{2}$$

where, H_i, K_i, and L_i ($i = 1, 2, 3$) are all unknown integers which can be determined using the trial and error method with a microcomputer. The structures decided by this method must be checked with many other diffraction patterns which are obtained at different tilt angles, the calculated diffraction data must coincide with the experimental results.

3. Results and Discussion

3.1 Crystallization behavior

The electron diffraction patterns of as-received material are all typical diffuse ring patterns, and no crystalline phases were observed.

The brightness of the bright field images become weaker and weaker during heating, even though the intensity of the incident electron beam was kept about the same. This variation of the brightness can be accounted for by the change of the amorphous structure. Due to the ordering of atoms in the specimen, the intensity of the diffracted beams increased and the transmitted beam decreased accordingly. However, it was impossible to detect quantitatively the ordering of atoms occurring in our experiments.

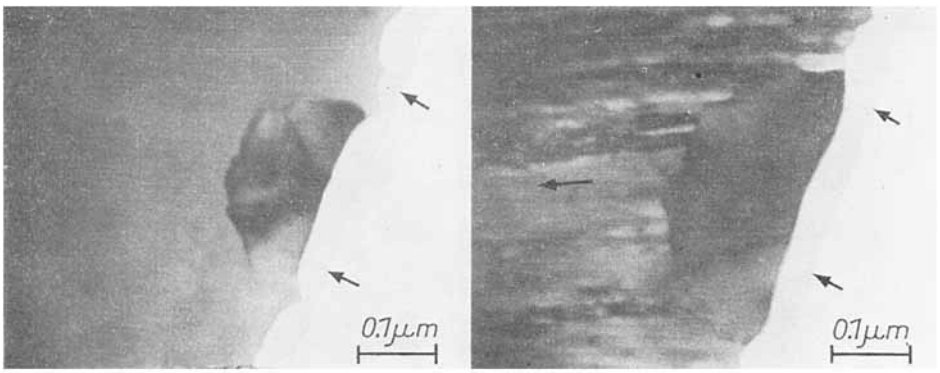

Fig. 1. Oxidation film and crystallization of the matrix. "→" shows the edge of the oxidation film. a) 395 °C, a metastable phase appeared at the edge of the matrix; b) 10 s later, rapid crystallization of the matrix around the metastable phase, the arrow shows the extension direction of the crystallized region

When the temperature of the specimen was raised to about 120 °C in the heating stage, a transparent layer began to appear at the edge and at the thinner regions of the specimens, and extended towards the matrix of the specimen continuously as the temperature of the specimen increased. These specimens heated in the TEM were analysed by means of Auger electron spectroscpoy (AES) which revealed that these transparent films were oxidation films formed during heating in the TEM [8].

When the temperature reached about 345 °C, metastable phases began to appear at the edge of the specimen and also in the thinner regions or near cracks. The nucleations of these metastable phases generally occurred separately at different local sites with different structures, with the exception of MS A and MS D which appeared diffusely over quite a large area. The details of these metastable phases will be recounted in the following section.

At a temperature of about 400 °C, the amorphous matrix began to crystallize at high speed with a definite crystallization front, which often started from the interfaces of the amorphous matrix and the metastable phases (Fig. 1). The electron diffraction patterns taken from the regions of the amorphous matrix near the crystallization front are still diffuse rings, but their intensity distribution is different from that of the as-received specimens. Aside from the ordering of atoms in the matrix, the effect of the oxidation film should be taken into account for the change of the intensity distribution. It is therefore difficult to make a quantitative comparison.

The rapid crystallization can be explained by a so-called autocatalyzed reaction [4]. The exothermal behavior at crystallization plays an important role in the rapid crystallization stage. In both stages, the initial stage, in which some metastable phases formed with a nucleation and growth mechanism, and the rapid crystallization, amorphous and metastable phases coexist along a moving interface. Therefore, the crystallization observed in $Pd_{80}Si_{20}$ is a first-order transition according to morphology.

The rapidly crystallized regions show two different types of morphology, one has a lamellar appearance and the other has an appearance of spots, see Fig. 2. These two types of rapidly crystallized regions do not have any clear boundaries, they can change from one type of morphology to the another during crystallization. When two crystallization fronts meet, an evident boundary forms, and this boundary will disappear gradually during further heating, but the traces of the extension directions of crystal-

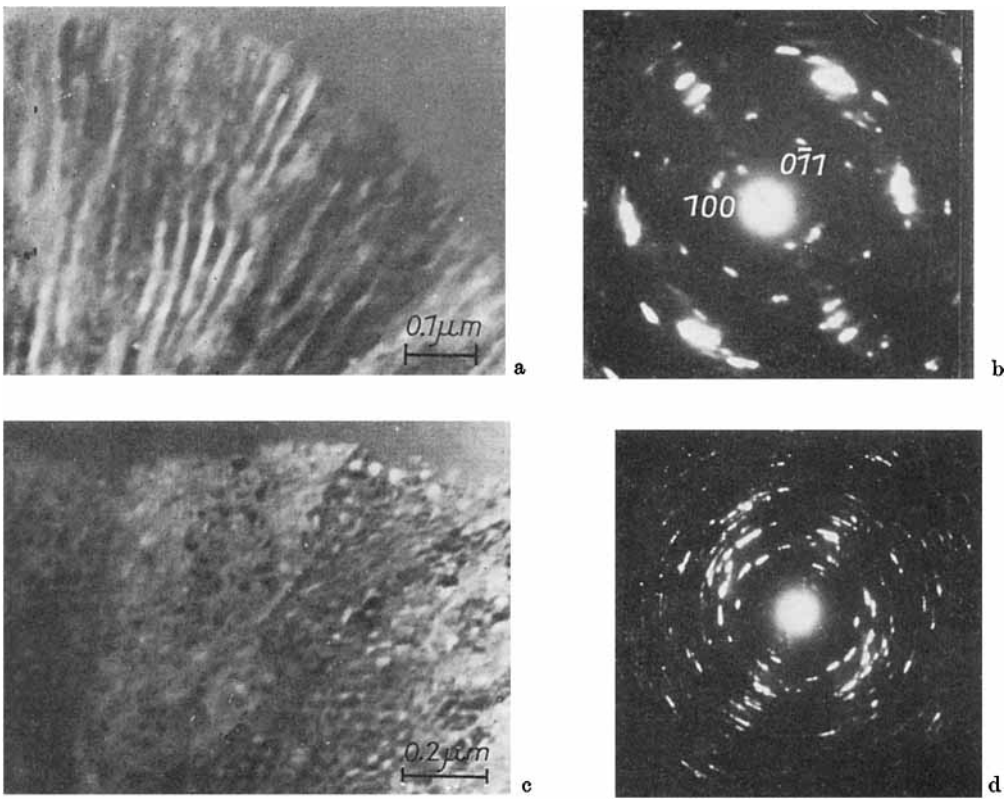

Fig. 2. The morphologies of rapidly crystallized regions and their electron diffraction patterns: a) lamella-like region; b) diffraction pattern of a), which contains the diffraction pattern of the [011] zone of Pd_3Si and the spots of Pd_3Si are indexed; c) spot-like region; d) diffraction pattern of c)

lized regions will still remain (Fig. 3). The morphologies at each side of the boundary in Fig. 3 have the characteristics of one of these two kinds of morphology each. The electron diffraction patterns taken from both sides of the boundary include that of the metastable phase E, and on side A contains the diffraction patterns of the [122] zone of Pd_3Si (Fig. 3b). It seems that these two types of rapidly crystallized regions have no essential difference. In the lamella-like regions, the diffraction patterns always contain the spot diffraction patterns of Pd_3Si and the extent of preferential orientation is much higher than that of another type of rapidly crystallized regions. The preferential orientations are different in different regions. The orientations of Pd_3Si observed in the lamella-like regions are [010], [110], [111], and [122] with respect to the normal of the specimens. The spot-like regions have no apparent preferential orientation and can be considered as sections of the lamella-like regions.

The electron diffraction patterns taken from the rapidly crystallized regions, which consist of Pd_3Si and MS E, show that the rapid crystallization has the character of an eutectic reaction and the eutectic cells consist of Pd_3Si and MS E. From the composition of the specimens, MS E should be a more palladium-rich silicide and the silicon content should be in the range of 14 to 18 at%. Besides, some diffraction patterns which contain weak diffraction rings of palladium were observed in some rapidly crystallized

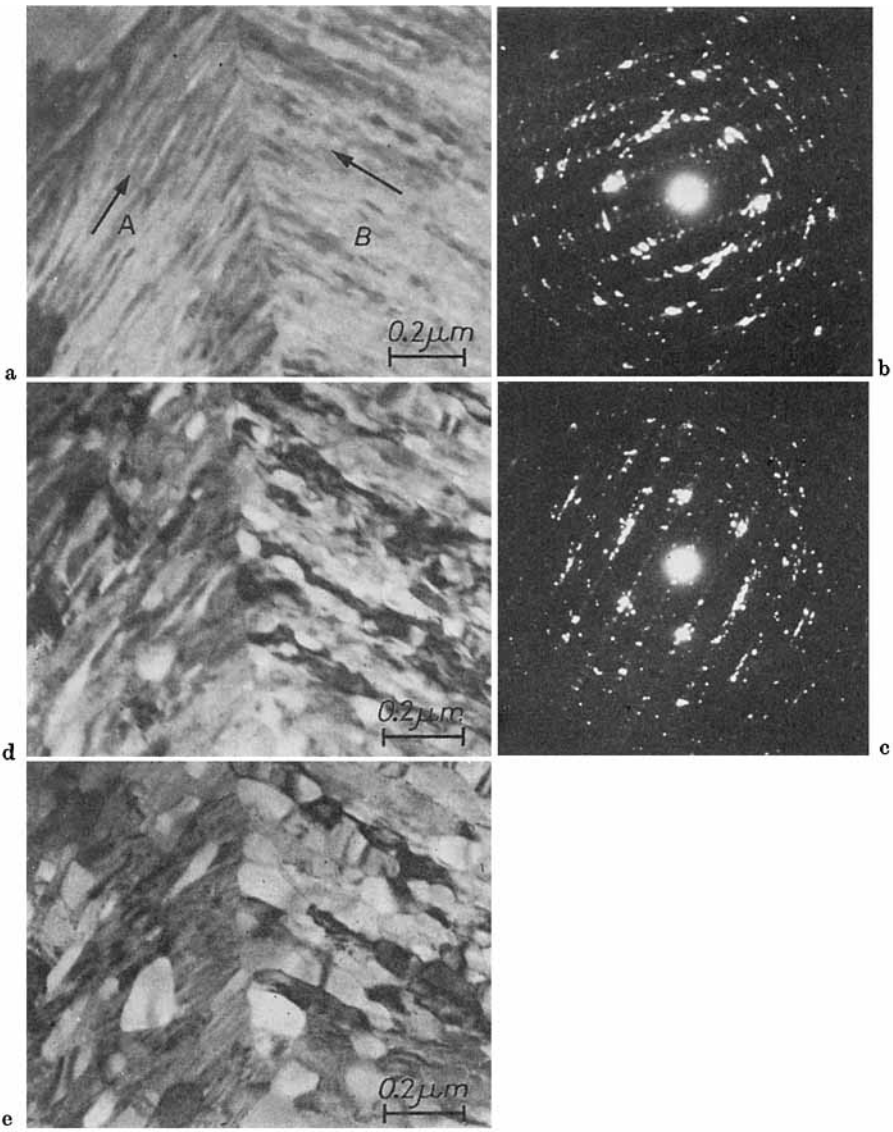

Fig. 3. A boundary formed by the meeting of two crystallization fronts. Arrows show the extension direction of crystallized regions: a) 400 °C; b), d) diffraction patterns at sides A and B in a), respectively; c) 420 °C; e) 440 °C

regions. Therefore, the X-ray diffraction data presented by Masumoto and Donvan et al. [1, 9] seem to be explained by Pd_3Si, MS E, and Pd.

A variety of moiré patterns have been observed at crystallized regions. Fig. 4 shows moiré patterns and the electron diffraction pattern taken from a moiré pattern area which contains that of the [111] zone of Pd_3Si. Moiré patterns are formed when the electron beam passes through a specimen where the upper and the lower parts have small misorientation and/or small spacing changes caused by different structures.

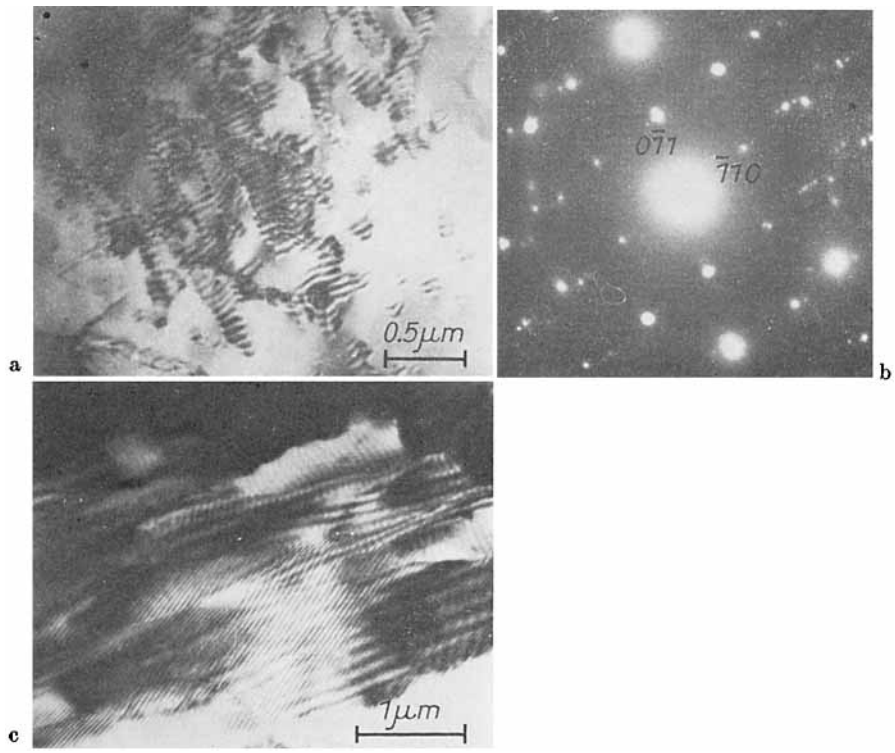

Fig. 4. Moiré patterns and diffraction pattern: a), c) Moiré patterns; b) electron diffraction pattern taken from the moiré pattern area of a), in which the diffraction spots of Pd_3Si have been indexed

From the origin of moiré patterns, we can conclude that the crystallization in the moiré pattern areas begins from the two surface layers of the specimen.

AES analysis results revealed that the composition of the surface layers varies during heating, i.e. silicon atoms diffuse inwards once a specimen has been heated [10]. Owing to this kind of diffusion, the content of palladium at the surface layers increased. Crystallization temperature and related properties of amorphous Pd–Si alloys depend critically on the silicon content of the alloys. It has been found by differential thermal analysis (DTA) and electrical resistivity measurements that the most stable Pd–Si alloy is $Pd_{82}Si_{18}$; an increase or decrease of the silicon content will make the amorphous state more unstable [4]. The directional diffusion of silicon atoms towards the interior of a specimen decreases the stability of the two surface layers, so crystallization begins just from both the surface layers and moiré patterns are formed.

At a temperature of about 450 °C, metastable phases begin to transform into stable phase Pd_3Si and Pd.

Therefore, the crystallization process of the amorphous $Pd_{80}Si_{20}$ alloy can be roughly summarized as follows: amorphous → ordering of atoms in the incipient stage → → amorphous + metastable phases appear at local regions → rapid crystallization with an eutectic reaction (Pd_3Si + MS E) + metastable phases → stable phase (Pd_3Si + Pd).

The experimental results show that structure relaxation or atom rearrangement occurs before the crystallization temperature is reached during heating. Owing to

oxidation and diffusion of atoms occurring at the surface layers, an increase of composition inhomogeneity at these layers will decreases the crystallization temperature and a variety of metastable phases will occur at some local sites. The number and the relative amount of these metastable phases vary with the oxidation and diffusion of atoms. Once rapid crystallization starts around these metastable phases, crystallized regions will extend rapidly in the manner of an eutectic reaction. When the heating temperature is high enough, these metastable phases will transform to the stable phases Pd_3Si and Pd. Duhaj and coworkers indicated that no metastable phases were formed during crystallization and only the morphology of the formed silicides, Pd_3Si and Pd_9Si_2, was unstable [2]. But our results show clearly that a number of metastable phases are formed during crystallization. There is a metastable stage between amorphous state and the stable phase. The existence of a number of metastable phases in the initial stage of crystallization observed in our experiments shows the complexity of crystallization from the amorphous state, which can transform to a stable phase through different metastable phases.

3.2 The structures of the metastable phases

In the range of 345 to 400 °C, a number of metastable phases have been observed during crystallization of metallic glass $Pd_{80}Si_{20}$. MS A and MS D are diffuse crystalline phases with ring diffraction patterns, which appeared over quite a large area at the temperature of 345 and 360 °C, respectively. MS A belongs to the f.c.c. structure with the parameter $a = 0.388$ nm, nearly the same as that of pure palladium, which was called MS I by Masumoto et al. [1]. This phase does not always appear evidently everywhere or in every specimen, and can be considered a precipitate of palladium from the amorphous matrix (Fig. 5). MS D is a b.c.c. structure with $a = 0.287$ nm, very close to the parameter of α-Fe, but the Auger analysis results show that there is not any trace of iron in the specimens used in the TEM observation, even during Ar^+ ion sputtering.

The electron diffraction patterns of other metastable phases are all spot diffraction patterns and used to analyse the structures of these metastable phases. For example, the structure of MS C was obtained using the method mentioned in Section 2, which is a triclinic structure with $a = 0.447$ nm, $b = 0.658$ nm, $c = 0.871$ nm, $\alpha = 96.9°$, $\beta = 90°$, $\gamma = 107.6°$. The theoretical data of diffraction patterns and these observed

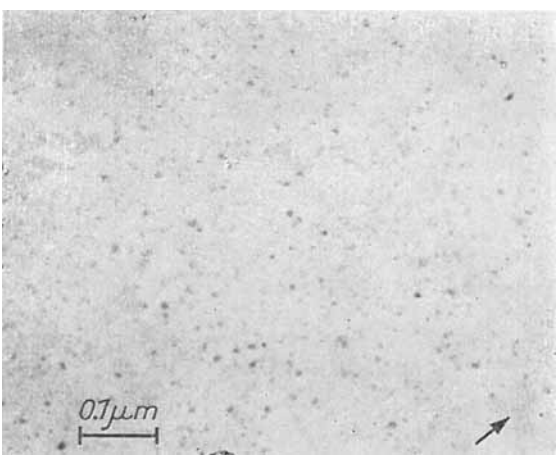

Fig. 5. Electron micrograph of MS A; a nucleus of MS B is shown by the arrow

Table 1
Comparison between the calculated diffraction data and the observed values

No.	g and the angle between $\boldsymbol{g}_1$ and $\boldsymbol{g}_2$			zone axis	index of g_1 and g_2		Laue spot and its projections		
	g_1 (nm^{-1})	g_2/g_1	φ (°)	uvw	$h_1k_1l_1$	$h_2k_2l_2$	hkl	g_x/g_1	g_y/g_2
1348	0.0469	1.17	95.3					0.76*	0.15*
	0.0468	1.199	96.68	$\bar{3}\bar{1}7$	$1\bar{3}0$	211	201	0.283	0.865
1349	0.0469	1.04	79.8					0.68*	0.17*
	0.0468	1.043	81.06	$\bar{3}\bar{1}6$	$1\bar{3}0$	201	$2\bar{1}1$	0.327	0.845
1350	0.0469	1.01	118.8					0.82*	0.61*
	0.0462	1.013	118.01	$\bar{3}\bar{1}5$	$\bar{2}1\bar{1}$	$1\bar{3}0$	$0\bar{1}0$	0.181	0.386
1351	0.0350	1.34	72.3					0.23	0.22
	0.0352	1.328	71.88	$\bar{3}\bar{1}4$	$1\bar{1}1$	$1\bar{3}0$	$0\bar{1}0$	0.216	0.251
1352	0.0257	1.83	96.2					0.26	0.30
	0.0266	1.760	96.81	$\bar{3}\bar{1}3$	$10\bar{1}$	$1\bar{3}0$	$0\bar{1}0$	0.262	0.319
1354	0.0469	1.05	66.5					0.17	0.43
	0.0468	1.075	66.06	$\bar{6}\bar{2}5$	$1\bar{3}0$	$2\bar{1}2$	$1\bar{1}1$	0.183	0.428
1355	0.0254	1.42	97.5					0.95*	0.42*
	0.0262	1.354	97.35	$\bar{3}\bar{1}2$	$1\bar{1}1$	021	011	0.102	0.581
1357	0.0163	1.58	108.0						
	0.0161	1.499	107.69	001	$0\bar{1}0$	100	201	0.909	1.000

in the experimental diffraction patterns, as an example, are shown in Table 1. The first rows for every pattern in Table 1 are the observed values, and the second rows are the calculated data. g_1's and g_2's are the lengths of the shortest and the next shortest reciprocal lattice vectors, $[h_1k_1l_1]^*$ and $[h_2k_2l_2]^*$, on the $(uvw)^*$ reciprocal lattice plane, respectively. φ is the angle between $\boldsymbol{g}_1$ and $\boldsymbol{g}_2$. (hkl) is the index of the first-order Laue spot, the projections of which in the parallelogram formed by $\boldsymbol{g}_1$ and $\boldsymbol{g}_2$ on the zero-order $(uvw)^*$ plane are g_x and g_y. The stars "*" used for g_x/g_1 and g_y/g_2 indicate that the projections are that of -1-order Laue spots. The projection of $+1$-order Laue spots can be easily obtained from $g_x^{+1}/g_1 = 1 - g_x^{-1}/g_1$ and $g_y^{+1}/g_2 = 1 - g_y^{-1}/g_2$. It can be seen from Table 1 that these patterns were obtained by tilting the crystal around $[1\bar{3}0]^*$ in the reciprocal lattice space, and the observed values coincide very well with the calculated ones.

Fig. 6 shows the electron micrograph and some of the diffraction patterns of MS C. From all of the diffraction patterns, streaks are always seen passing through $[0kl]^*$. Diffraction streaks can be caused by planar defects (e.g., stacking faults, plate-like precipitates, etc.), but these streaks can appear only for certain electron incidence directions with respect to these planar defects and transform to spots when electron incidence deviates from particular directions. Whereas, there were neither plate-like precipitates nor stacking faults observed in the crystals (Fig. 6a), and the long spikes are always along $[0kl]^*$. A reasonable explanation for these streaks appearing in diffraction patterns is that $(100)^*$ planes in the reciprocal lattice space are planes of diffuse intensity which may be caused by a deviation of some kind of atoms, probably silicon atoms, from the equilibrium sites in the [100] direction in the real lattice space.

The structures of the metastable phases of $Pd_{80}Si_{20}$ obserbed during heating are summarized in Table 2.

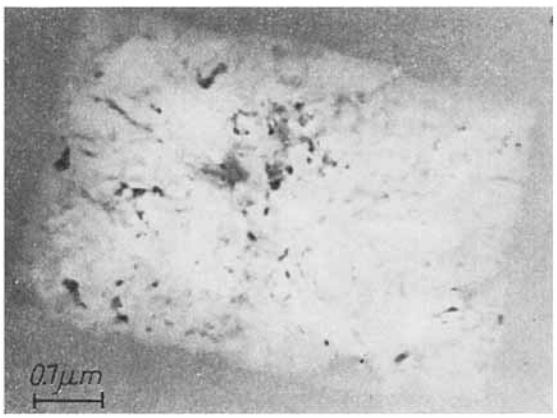

a

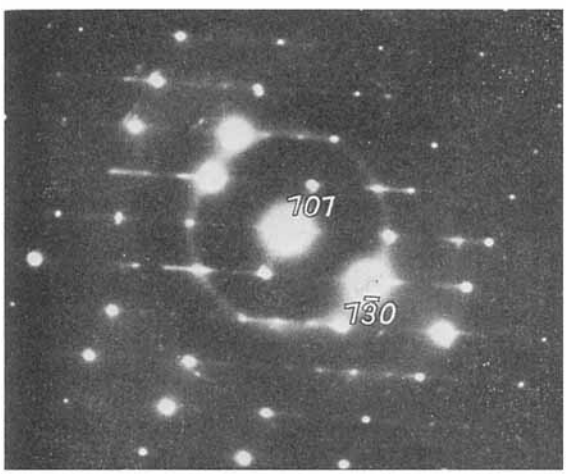

b

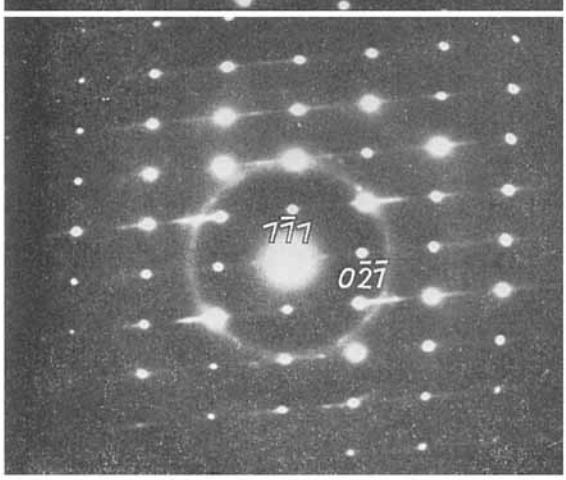

c

Fig. 6. Electron micrograph and diffraction patterns of MS C:
a) electron micrograph; b), c) diffraction patterns of [001] and [312] zones, respectively

Table 2
The metastable phases of metallic glass $Pd_{80}Si_{20}$

phase	structure	structure parameters					
		a	b	c (nm)	α	β	γ (°)
MS A	f.c.c.	0.388					
MS B	pseudo ortho-rhombic	1.329	1.638	0.605	90.4	90.6	91.1
MS C	triclinic	0.447	0.658	0.871	96.9	90	107.6
MS D	b.c.c.	0.287					
MS E	monoclinic	1.664	0.474	2.416		94.1	
MS F	hexagonal with an irregular spacing in c	0.719					
MS G	superstructure based on hexagon	0.272					

3.3 Some characteristics of metastable phases

Some metastable phases have unconventional structures, which are reflected from their electron diffraction patterns. The diffraction patterns of MS F vary continuously during tilting the crystal, that is, the basal parallelogram, which consists of the shortest and the next shortest reciprocal lattice vectors in the electron diffraction patterns, does not vary evidently; some of the diffraction patterns are shown in Fig. 7. The diffraction pattern at zero tilt angle clearly displays the sixfold (or threefold) axis characteristics (Fig. 7 a). From this symmetry, it can be seen that this metastable phase can only be of cubic, rhombohedral, or hexagonal structure. The tilt axis used in our experiment is parallel to [211]* in cubic or rhombohedral structure, and to [$\bar{2}$10]* in hexagonal structure. If this metastable phase were cubic or rhombohedral, the diffraction pattern would have changed to a quite different one when the crystal was tilted about 10° around [211]*. The diffraction patterns obtained here show that this metastable phase has a special hexagonal structure; its reciprocal lattice points become continual

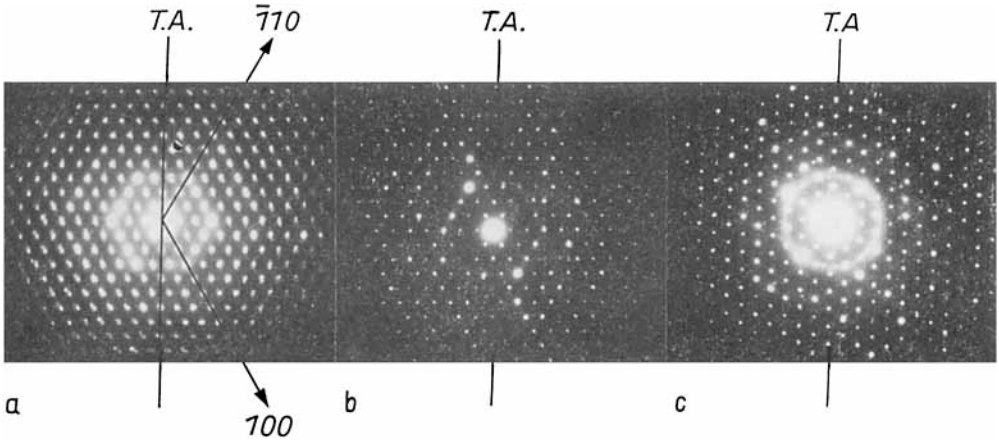

Fig. 7. Electron diffraction patterns of MS F at different tilt angles; the tilt axis is shown by marks: a) 0°, b) 10°; c) 20°. T. A. tilt axis

Table 3
Angles between so-called [100]* and [$\bar{1}$10]* for MS F

tilt angle	0°	10°	20°	30°
φ_0 (observed)	120°	119.2°	117.2°	113.5°
φ_c (calculated)	120°	119.24°	116.87°	112.62°

spikes in the direction $\boldsymbol{c}^*$ in the reciprocal lattice space, so that the angle between [100]* and [$\bar{1}$10]* varies continuously following the change of the tilt angle. Table 3 shows the observed angles φ_0 between [100]* and [$\bar{1}$10]*, and the values φ_c which were calculated from the continuum model of the reciprocal lattice points; they coincide with each other very well.

These continuous reciprocal lattice spikes can be interpreted by irregular separations of the lattice planes in direction $\boldsymbol{c}$. The crystals are composed of parallel identical planes of atoms, or layers consisting of several planar arrays of atoms with regular interplanar spacing, which are stacked in such a way that the spacing between them is not fixed. This model has been used to explain the structures of some crystals of clay minerals [11], and it can be used to explain the structure of MS F, too. The Pd and Si atoms in the binary alloy $Pd_{80}Si_{20}$ form two-dimensional infinite planes of atoms according to some stoichiometry during crystallization; the extra atoms (Pd or Si) lie in the spaces between two identical sheets of atoms, and the bonding between two sheets is different from that in the same sheet. The thickness of these sheets and the spaces between two sheets are not fixed. Si atoms diffuse from the surface layers towards the interior of a specimen during heating and cause a composition gradient from the surface to the interior [10], so that it is advantage to form a structure like MS F. We have observed this kind of structure during crystallization of metallic glass CoFeNiSiB and found that (001) is a pseudo-cleavage plane [12]. It indicates that the proposed structure model is reasonable one.

The stoichiometric structures that have been found in Pd–Si alloys are PdSi, Pd_2Si, Pd_3Si, Pd_4Si, and Pd_9Si_2, among which only Pd_2Si has hexagonal structure with $a = 0.6496$ nm, $c = 0.3433$ nm [13]. The difference between a in MS F and Pd_2Si is 0.069 nm (10.6%). We suppose that "the normal sheet" (i.e. the stoichiometric part) is Pd_2Si, since the bonding between these sheets varies, the value of "a" in the sheets is different from that of Pd_2Si. The extra Pd atoms stack in the spaces between these sheets and modify the distance between these sheets without affecting their relative orientations.

An unconventional superstructure metastable phase, MS G, forms during crystallization. There are always eleven weak spots between two strong spots in the diffraction patterns, in which the strong spots are similar to that of MS F and all the weak spots lie on (110)* of the reciprocal lattice of the strong diffraction. The diffraction pattern and the intensity distribution in the reciprocal lattice space are shown in Fig. 8. The weak spots result from an orthorhombic superstructure with $a = 1.632$ nm, $b = 0.471$ nm. This superstructure has an irregular repeating period in c-direction, too. Fig. 8c is a (100) lattice image of the superstructure.

In the diffraction patterns of some metastable phases, e.g. MS B, many subsidiary spots with a comparable intensity appear regularly. The reciprocal lattice can be worked out from the diffraction patterns [14], in which the c^*-axis is much larger than a^*- and b^*-axes, and the reciprocal lattice points are elongated along the c^*-direction. So that, when the Ewald sphere intersects the reciprocal lattice, it intersects not only these reciprocal lattice points, which align on a reciprocal plane, but also the points on

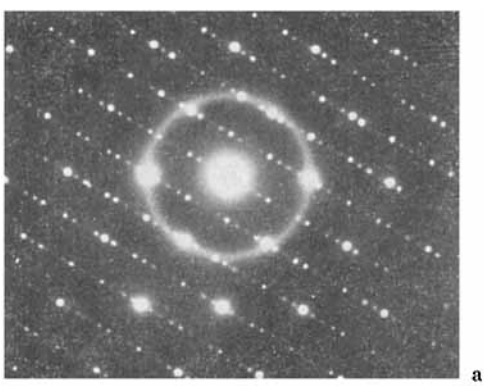

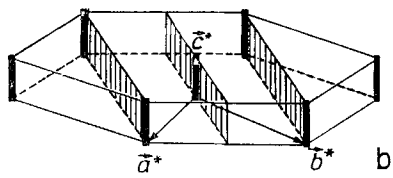

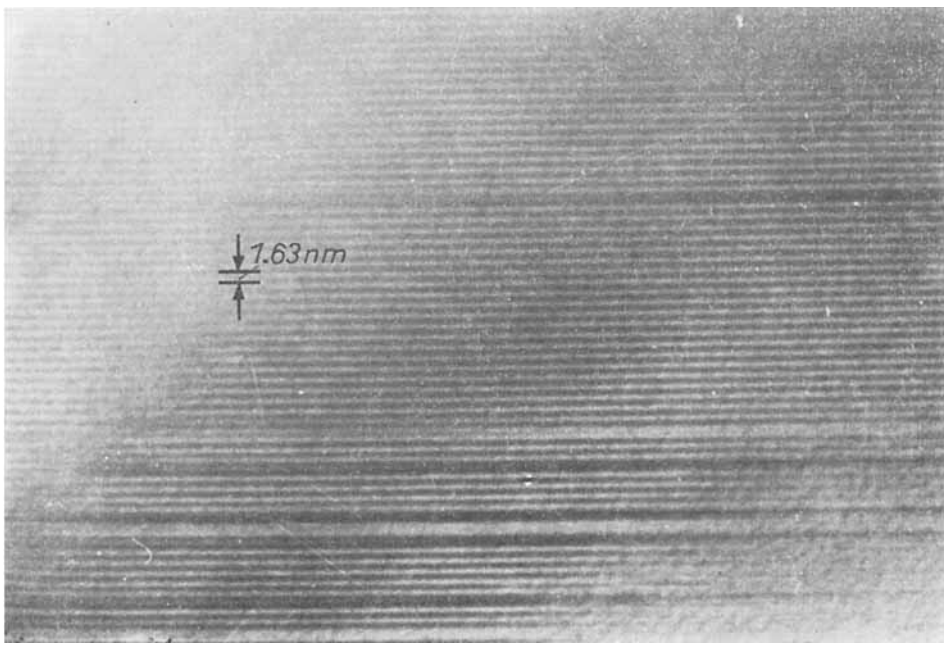

Fig. 8. Electron diffraction pattern and high resolution image of MS G: a) diffraction pattern; b) schematic illustration of the intensity distribution in the reciprocal lattice space; c) (100) lattice image of the superstructure, some structural imperfections can be seen from the change of the fringe spacing

the neighbor planes. Therefore, subsidiary rows of spots with a comparable intensity appear in the diffraction patterns. The elongation of reciprocal lattice points in direction $\boldsymbol{c}^*$ can be related to some kind of structural imperfections. It has been found in high resolution images that the displacement of lattice fringes elongates the reciprocal lattice points in the corresponding direction in the reciprocal lattice space. The local displacements of the lattice in c-direction make the parameter c just as if it were an average value, and cause the reciprocal lattice points to be elongated in the direction $\boldsymbol{c}^*$. Since the subsidary diffraction spots are related with the structural imperfections of a crystal, the distributions of the subsidary diffraction spots are quite different for different crystals, as is shown in Fig. 9.

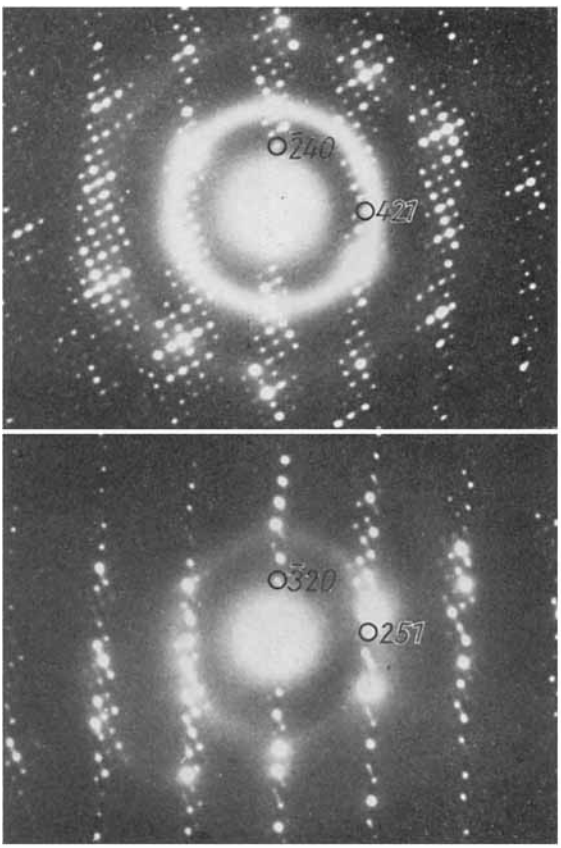

Fig. 9. Diffraction patterns obtained from two crystals of MS B: a) [$\bar{1}\,\bar{2}\,12$] zone of one crystal; b) [$\bar{2}\,\bar{1}\,10$] zone of another crystal

It has been found that if the difference between one of the axes and the others is large enough, or an anomalous axis exists for a metastable phase, this axis always nearly parallels the normal of the specimen, e.g. the c-axis of MS B, MS E, MS F, and MS G. It shows the size effect of specimens for crystallization, which may be caused by the directional diffusion of silicon atoms during heating or left from producing the ribbons.

High resolution lattice images can directly reveal the lattice defects and structural imperfections of the metastable phases. Fig. 10 shows a low-angle boundary and some dislocations. From the change of lattice fringes, one lattice fringe became two in Fig. 10 and two lattice fringes became three in Fig. 11, the structural imperfections are presented directly.

Different structures can coexist in a small crystallized region. In Fig. 11, two types of fringes with different spacings which show two types of structures coexist in that region. In some crystallized regions small zones, where the lattice fringes do not continue and their contrast is different from that of the surrounding areas, can be observed. These small zones, shown by arrows in Fig. 11, may be amorphous islands which were left during crystallization owing to the local inhomogeneity of composition.

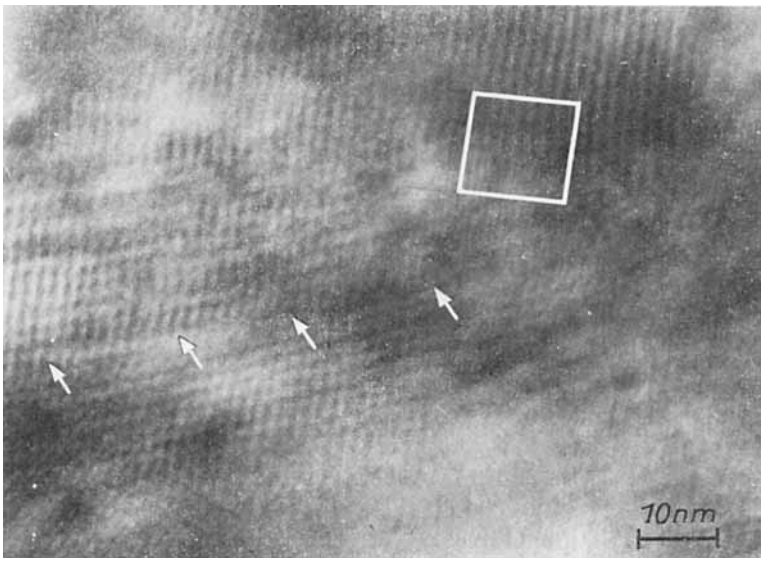

Fig. 10. Lattice defects in metastable phase. Arrows show the dislocations which form a low-angle-boundary. The change of the spacing of the fringes is shown in a frame

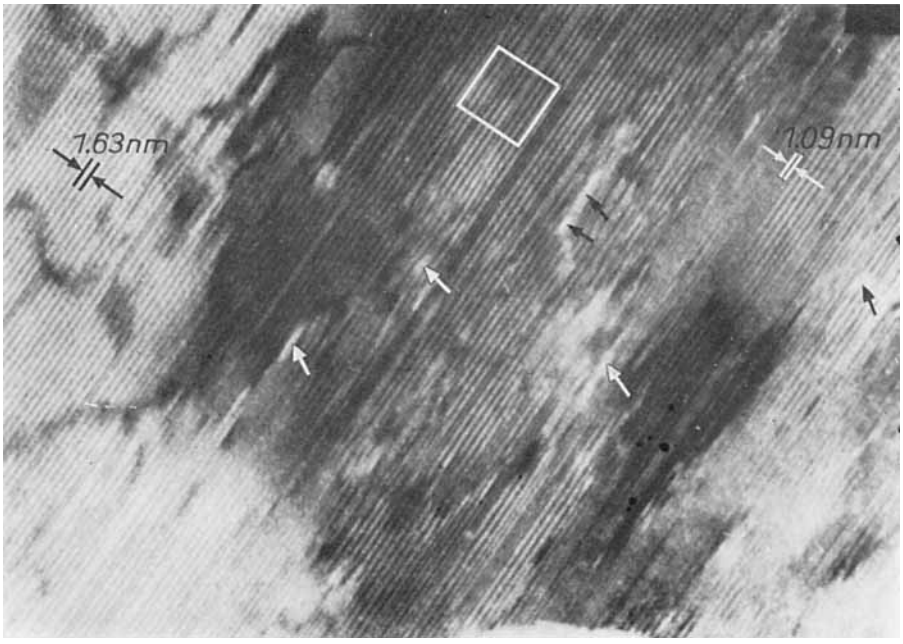

Fig. 11. Structural imperfections in a metastable phase. Arrows show the amorphous islands, the spacing between fringes varies in the frame

4. Conclusion

The crystallization behavior of amorphous $Pd_{80}Si_{20}$ has been studied by in situ observation during heating in TEM. The crystallization is carried out with four stages which is summarized as follows:

1) ordering or rearrangement of atoms in the amorphous matrix;

2) a variety of metastable phases with different structures appear at local sites in the amorphous matrix;

3) rapid crystallization of the remaining amorphous matrix with an eutectic reaction, the eutectic cells consist of Pd_3Si, and a metastable phase with monoclinic structure;

4) metastable phases transform to stable phases Pd_3Si and Pd.

Metastable phases are a transition stage from the amorphous state to a stable phase, and their nucleation and growth are affected by many factors. The diffusion of Si atoms from the surface layers towards the interior of the specimens and the surface oxidation occurring during heating have a large effect on the crystallization of amorphous Pd–Si alloys. Therefore, many metastable phases appear at different regions during heating, and it is easy for metastable phases to form structural imperfections. The structural imperfections in some metastable phases cause the electron diffraction patterns of these phases to have their own features.

Acknowledgement

We would like to thank Dr. R. W. Siegel for reviewing the manuscript.

References

[1] T. Masumoto and R. Maddin, Acta metall. **19**, 725 (1971).
[2] P. Duhaj, V. Sládek, and P. Mrafko, J. non-cryst. Solids **13**, 341 (1973/74).
[3] P. Duhaj, D. Barančok, and A. Ondrejka, J. non-cryst. Solids **21**, 411 (1976).
[4] N. Funakoshi, T. Kanamori, and T. Manabe, Japan. J. appl. Phys. **17**, 11 (1978).
[5] P. Duwez, R. H. Willens, and R. C. Crewdson, J. appl. Phys. **36**, 2267 (1965).
[6] H. S. Chen and C. E. Miller, J. Sci. Instrum. **41**, 1237 (1970).
[7] Researchers of EM Laboratory, Institute of Metal Research, Acta metall. Sinica **13**, 73 (1977).
[8] Li Zongquan, Qi Zhenzhong, and He Yizhen, Acta metall. Sinica, to be published.
[9] P. E. Donvan and W. M. Stobbs, Mater. Sci. Eng. **19**, 1 (1975).
[10] Li Zongquan and He Yizhen, KEXUE TONGBO (Chinese Science Bulletin) **30**, 1859 (1985).
[11] J. M. Cowley, Diffraction Physics, North-Holland Publ. Co., Amsterdam 1981 (p. 152).
[12] Li Zongquan and He Yizhen, to be published.
[13] A. Nylund, Acta chem. Scand. **20**, 2381 (1966).
[14] Li Zongquan, J. Chinese Electron Microscopy Society, to be published.

(Received August 27, 1986)